



3D ordered MoP inverse opals deposited with CdS quantum dots for enhanced visible light photocatalytic activity



Yun Song^a, Najun Li^{a,b,*}, Dongyun Chen^{a,b}, Qingfeng Xu^{a,b}, Hua Li^a, Jinghui He^a, Jianmei Lu^{a,b}

^a College of Chemistry, Chemical Engineering and Materials Science, Collaborative Innovation Center of Suzhou Nano Science and Technology, Soochow University, Suzhou, Jiangsu 215123, China

^b State and Local Joint Engineering Laboratory for Novel Functional Polymeric Materials, Suzhou, Jiangsu 215123, China

ARTICLE INFO

Keywords:

CdS quantum dots
MoP inverse opals
Phenol degradation
Visible-light-driven photocatalyst

ABSTRACT

A novel three-dimensional ordered nanoheterojunctions are fabricated and proposed in photocatalytic phenol degradation. CdS quantum dots (CdS QDs) are adopted as light harvesters for good visible light absorption capacity, and MoP inverse opals (MoP IO) are applied as cocatalysts for excellent electrical conductivity. The introduction of three-dimensional ordered MoP is beneficial to expose active sites and improve the light absorption efficiency of heterojunctions. Effects of pore sizes and deposited amounts of CdS quantum dots are investigated and optimal conditions are obtained. The optimal pseudo-first-order reaction rate constants of CdS/MoP IO is $2.912 \times 10^{-2} \text{ min}^{-1}$, which is 7.7 times higher than pure CdS QDs, indicating the heterojunctions effectively reduce the photocorrosion of CdS QDs. CdS/MoP IO exhibit efficient charge carriers separation and favorable stability, which might provide new insights into environmental remediation and solar energy conversion.

1. Introduction

Phenol, as a precursor, is commonly applied in many industries, and it is a typical pollutant in industrial wastewater [1–4]. Phenol has serious impacts on ecological environments and is considered as harmful organic contaminant for its carcinogenic characteristic. Conventional treatments such as physical adsorption [5,6], coagulation [7,8] and extraction [9,10] have been applied to remove phenol in wastewater. Nevertheless, these conventional strategies do not completely degrade phenol. Therefore, it is urgent to develop an efficient and environmentally friendly technology to remove phenol from effluent. In recent years, semiconductor photocatalytic technique applied in water splitting and degradation of organic contaminants has received much attention [11–16], and it is expected to address the global energy and environmental issues. Among various semiconductors, CdS has been greatly studied for photocatalytic reactions because of its efficient visible light absorption [17–19]. Cadmium sulfide with quantum dots nanostructures are recognized as ideal photocatalysts because their band structure can be accurately modified by adjusting the size of quantum dots [20–22]. However, there are still some defects that prohibit its wide applications such as inefficient separation of photo-generated charge carriers and photocorrosion effect. Therefore, it is of

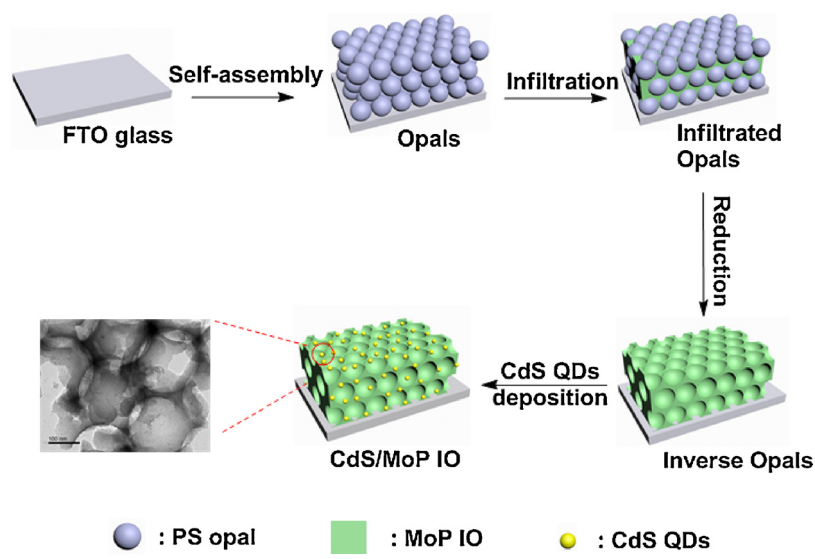
great significance to employ appropriate cocatalysts to enhance the activity of CdS QDs. Platinum [20,23,24] and palladium [25] are usually efficient cocatalysts for photocatalytic systems, but they are expensive and rare which probably inhibits their practical application.

Recently, transition metal phosphides (e.g., MoP [26,27], Ni₂P [28,29], CoP [30,31], FeP [32]) have been prepared for photocatalysts. MoP was adopted as co-catalyst for high electrical conductivity, favorable stability and superior catalytic activities. Yin [26] et al. prepared MoP nanoparticles sized around 10–30 nm by probe ultrasonication process to expose more active sites, and combined with CdS QDs as light harvesters. The highest H₂ evolution rate of 1100 $\mu\text{mol h}^{-1}$ can be obtained by this photocatalytic system. Du [27] et al. synthesized MoP nanoparticles attached on CdS nanorods, this heterojunction effectively reduced recombination of charge carriers and performed highly efficient H₂ evolution. However, there have been no report about three-dimensional (3D) ordered MoP inverse opals employed in photocatalytic system. Inverse opal is considered as a promising photocatalyst because of its high specific surface area and excellent light absorption properties [33–35]. Slow photons effect of inverse opals can efficiently increase the optical path length and thereby enhance light-harvesting efficiency of photocatalysts.

In this work, we have developed a facile method for CdS quantum

* Corresponding authors at: College of Chemistry, Chemical Engineering and Materials Science, Collaborative Innovation Center of Suzhou Nano Science and Technology, Soochow University, Suzhou, Jiangsu, 215123, China.

E-mail addresses: linajun@suda.edu.cn (N. Li), lujm@suda.edu.cn (J. Lu).



Scheme 1. Schematic illustration of the synthesis of CdS/MoP IO.

dots-deposited molybdenum phosphide inverse opals photocatalysts (**Scheme 1**). MoP IO are prepared by filling the restricted gap of polystyrene templates and reduction with a H_2 flow. The as-synthesized CdS quantum dots, performed as light harvesters, are fully commixed with MoP IO and calcined to obtain composites. The photocatalytic performance of CdS/MoP IO is evaluated by phenol degradation. As we know, activities of photocatalysts are influenced by photoabsorption abilities, separation of charge carriers and so on. Compared to CdS QDs, improved photocatalytic degradation efficiency of CdS/MoP IO heterostructures can be obtained for the synergic effect of fast mobility of photoexcited electrons and holes pairs and improved light-harvesting properties. The active species in photocatalytic phenol degradation by CdS/MoP IO are studied, and its probable mechanism is tentatively probed. Besides, the CdS/MoP IO heterostructures perform favorable photo-stability and durability attributed to reduced charge recombination. It is hoped that our research will provide new insights into photocatalytic environmental remediation.

2. Experimental section

2.1. Materials

Polyvinylpyrrolidone K30 (PVP), styrene, cadmium oxide (CdO), oleic acid, 1-octadecene, 3-mercaptopropionic acid (MPA), tetramethylammonium hydroxide pentahydrate (TMAOH) and ammonium heptamolybdate tetrahydrate ($(NH_4)_6Mo_7O_{24} \cdot 4H_2O$) were purchased from Sigma Aldrich. Potassium persulfate, elemental sulfur (S), anhydrous ethanol ($> 99.7\%$) and diammonium hydrogen phosphate ($(NH_4)_2HPO_4$) were purchased from Sinopharm Chemical Reagent Co. Ltd. Fluorine-doped tin oxide (FTO) glass were obtained from Kun Shan Jia Yi Sheng Co., Ltd.

2.2. Characterization

Scanning electron microscopy (SEM, Hitachi SU8010) was applied to analyze the morphology of all the samples. The transmission electron microscopy (TEM) images, high-resolution TEM (HRTEM) images and elemental mapping were performed on Hitachi H600. X-Ray powder diffraction (XRD) patterns were performed on X' Pert-Pro MPD with Cu K α radiation. X-ray photoelectron spectroscopy (XPS) was measured by ESCALAB MK II with Al-K α radiation. Ultraviolet visible (UV-vis) spectra were measured by Shimadzu UV-3600. The photoluminescence (PL) emission spectra were obtained from a FLS920 fluorescence

spectrophotometer. The concentration of phenol was analyzed by high-performance liquid chromatography (HPLC, Agilent 1260). Total organic carbon (TOC) was tested using a TOC analyzer (TOC-L CPH CN200, Shimadzu). Electron spin-resonance spectroscopy (EPR, JEOL JES-X320) was used to detect radicals spin-trapped by 5,5'-dimethyl-1-pyrroline-N-oxide (DMPO) of which center field (326 mT), microwave frequency (9.15 GHz), and power (20 mW) are set.

2.3. Fabrication of photocatalyst (CdS/MoP IO)

2.3.1. Preparation of MoP IO

The monodisperse PS particles were synthesized by emulsifier-free emulsion polymerization as reported elsewhere [36]. PS spheres with different diameters of 130 nm, 280 nm and 420 nm (indexed as PS130, PS280 and PS420) were prepared by using different amount of surfactants. PS spheres were assembled onto the fluorine-doped tin oxide (FTO) glass substrate via a vertical deposition method to prepare PS opals. Subsequently, 0.1766 g $(NH_4)_6Mo_7O_{24} \cdot 4H_2O$ and 0.1321 g $(NH_4)_2HPO_4$ were dissolved in 10 mL deionized water, the solution was stirred for 30 min and indexed as MoP precursor solution. PS opals were first infiltrated into MoP precursor solution at 60 °C for 1 h and calcined at 500 °C for 3 h. Then the FTO glass were calcined at 750 °C under a H_2 flow for 2 h with a heating rate of 2 °C/min followed by heated at 200 °C for 1 h under an Ar atmosphere.

2.3.2. Preparation of CdS/MoP IO

CdS QDs were synthesized by a hot injection method with a little modification. Briefly, 0.1280 g CdO and 1.3293 g oleic acid was added to 34.6506 g octadecene and heated to 280 °C. 0.0160 g sulfur was dissolved in 3.95 g octadecene and injected into the hot solution above. The mixture was maintained at 250 °C for 10 min to grow CdS QDs and rapidly cooled to 60 °C. 20 mL of CH_3OH/CH_3COCH_3 (1:1) was used to precipitate nanocrystals. CdS QDs were further transferred into water by mercaptopropionic acid. Then the obtained CdS QDs and MoP IO were homogeneously mixed and calcined at 200 °C for 2 h.

2.4. Photocatalytic activity test

The photocatalytic activity of CdS/MoP IO was evaluated by degradation of phenol under visible-light illumination. 20 mg photocatalyst was dispersed in 50 mL of 20 mg/L phenol solution. Before illumination, the suspension was stirred in dark for 2 h to achieve absorption-desorption equilibrium (Figure S1). And then the suspension

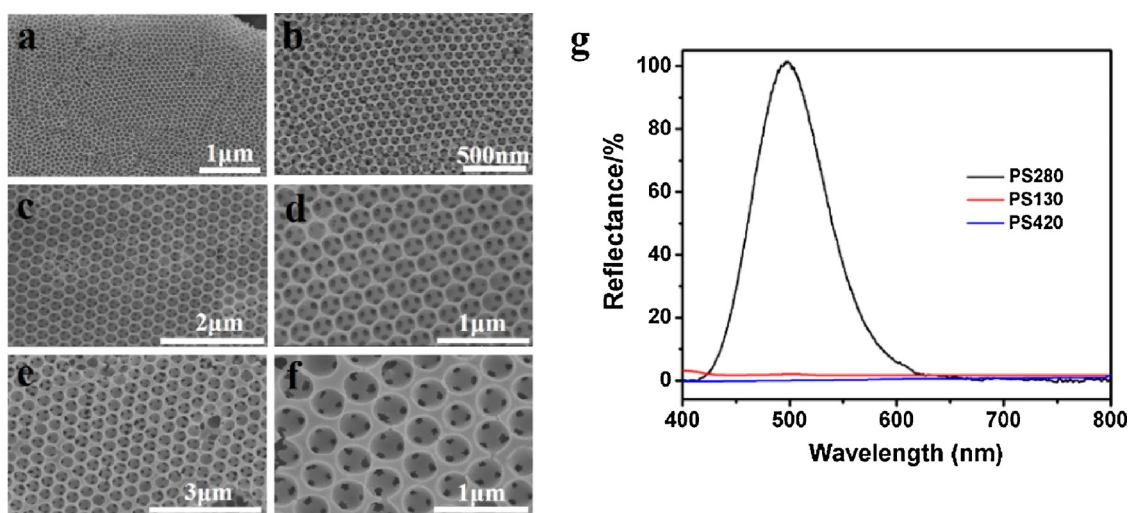


Fig. 1. SEM images of CdS/MoP IO with different air cavity diameters obtained from PS130 (a, b), PS280 (c, d) and PS420 (e, f) and reflectance spectra of CdS/MoP IO (g).

was irradiated by a Xenon lamp source (with a light filter > 420 nm) and 1 mL suspension was collected and centrifuged at regular intervals to analyze the concentration of phenol. The phenol concentrations were determined by high-performance liquid chromatography.

3. Results and discussion

3.1. Effect of air cavity diameter

PS with different diameters are synthesized and self-assembled to PS opals (PS130, PS280 and PS420) as shown in Figure S2. Since PS opals are burned off, the air cavities of CdS/MoP IO are contracted in Fig. 1. The morphologies of CdS/MoP IO are similar with pure MoP IO (Figure S3), indicating the introduction of CdS QDs doesn't change the microstructures of the composites. According to the reflectance spectra of CdS/MoP IO (Fig. 1g), only CdS/MoP IO prepared from PS280 exhibits a reflectance peak centered at 498 nm in visible-light region. The stop band reflection peak reveals that when composites absorbs incident photons near the band edges, the group velocity of incident photons decreases obviously, resulting in contacted interaction of photocatalysts and improved light absorption. Hence, CdS/MoP IO prepared from PS280 is selected for further investigation.

3.2. Characterization of CdS/MoP IO composites

MoP inverse opals with different depositing amount of CdS quantum dots (indexed as CdS(x)/MoP IO, $x \approx 20, 30$ and 40 wt%, respectively) are displayed in Fig. 2. As is shown in Fig. 2a-b, CdS quantum dots are less dispersed and cannot be uniformly deposited on the inverse opal skeleton. When the depositing amount is 40%, apparent aggregation of CdS quantum dots occurs (Fig. 2e-f). Therefore, an appropriate proportion of CdS QDs deposition on MoP IO is important. From Fig. 2c-d, CdS QDs are homogeneously distributed on the framework of inverse opal and form closely contacted nanocomposites. What's more, the cross-sectional SEM image of 30% CdS/MoP IO is shown in Figure S4, and the thickness of 30% CdS/MoP IO is about 3 μm .

Fig. 3a illustrates the elemental mapping of 30% CdS/MoP IO, CdS QDs are homogeneously dispersed on the framework of MoP IO, which is consistent with the result of TEM images. Fig. 3b shows the XRD patterns of CdS QDs, MoP IO and CdS/MoP IO with different CdS QDs contents. For pure CdS QDs, three peaks at $26.5^\circ, 43.9^\circ, 51.9^\circ$ can be indexed to (111), (220), (311) crystal planes of CdS (PDF#89-0440). The pure MoP IO exhibits seven peaks at $27.9^\circ, 32.1^\circ, 43.1^\circ, 57.5^\circ, 46.9^\circ, 67.9^\circ, 74.3^\circ$, which correspond to the (001), (100), (101), (110),

(111), (102), (201) planes of hexagonal MoP (PDF#24-0771), respectively. When increasing the depositing contents of CdS QDs, the diffraction peaks of CdS/MoP IO composites are similar to that of pure MoP IO except for gradually decreased peak intensities at 32.1° and 43.1° , confirming the good stability of MoP IO to incorporate CdS QDs. The HRTEM image of 30% CdS/MoP IO (Fig. 3c) clearly demonstrates lattice fringes spacing of 0.34 and 0.28 nm, corresponding to the (111) and (100) planes of CdS and MoP, respectively. Moreover, the microstructure of pure CdS QDs is revealed in Fig. 3d, it can be found that the CdS QDs are dispersed uniformly and its average diameter is around 5 nm.

The compositions and chemical states of 30% CdS/MoP IO are examined by X-ray photoelectron spectroscopy (XPS), and the results are shown in Fig. 4. From Fig. 4a, the peaks at 227.7 eV and 230.9 eV belong to Mo $3d_{3/2}$ and Mo $3d_{5/2}$ of MoP respectively. Furthermore, the other two peaks at 228.6 eV/231.9 eV ($\text{Mo}^{4+} 3d_{3/2}/3d_{5/2}$) and 232.8 eV/234.7 eV ($\text{Mo}^{6+} 3d_{3/2}/3d_{5/2}$) can be ascribed to MoO_2 and MoO_3 . It should be pointed out that the high oxidation states of molybdenum can be attributed to the passivation process in preparation. There is no diffraction peak of molybdenum oxides in the XRD data, which means that the oxidation reaction occurs only on the surface of MoP. The P 2p spectrum (Fig. 4b) reveals two peaks at 128.9 eV and 129.8 eV which correspond to P $2p_{2/3}$ and P $2p_{1/3}$ species in MoP. The peak appearing at 133.4 eV is attributed to the presence of PO_4^{3-} , P_2O_5 , and H_3PO_3 on the surface. According to Fig. 4c-d, Cd 3d peaks at 411.9 eV/405.2 eV (Cd $3d_{5/2}/3d_{3/2}$) and S 2p peaks at 161.5 eV/162.6 eV (S $2p_{3/2}/2p_{1/2}$) identify the presence of CdS.

UV-vis absorption spectra and photoluminescence spectra are conducted to investigate the optical properties of CdS QDs, MoP IO and CdS/MoP IO. The pure CdS QDs exhibit an absorption edge at 503 nm in Fig. 5a, which are blue-shifted compared to the reported CdS nanorods because of the quantization size effects of quantum dots. MoP IO show a flat plot with high adsorption coefficient in UV-vis range. For CdS/MoP IO, there is no obvious shift of the absorption edges compared to that of CdS QDs. 20% CdS/MoP IO exhibit the highest absorption intensity above 503 nm and the absorption intensity above 503 nm is enhanced with the increasing content of MoP IO, indicating the incorporation of CdS QDs to MoP IO effectively enhance the light absorption ability of CdS QDs and reduce the photocorrosion of CdS QDs. Photoluminescence (PL) spectra of all the samples are demonstrated in Fig. 5b to study the charge carriers separation/recombination rates. As we know, the intensity of emission spectra depends on the recombination of photoexcited electrons and holes. The weaker the peak intensity, the lower the recombination rate of charge carriers. The

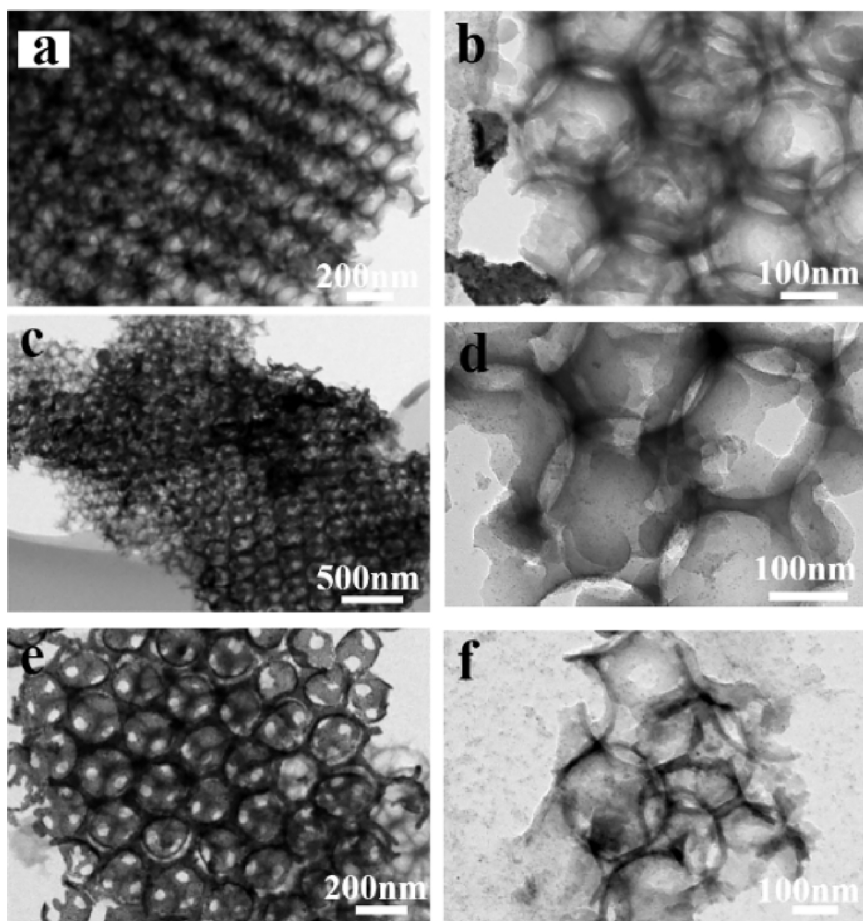


Fig. 2. TEM images of MoP inverse opals with different depositing amount of CdS QDs (a, b) 20%, (c, d) 30% and (e, f) 40%.

emission peak centered at 625 nm for CdS QDs can be attributed to the recombination of charge carriers in CdS QDs. Compared to CdS QDs, CdS/MoP IO show lower peak intensities which can be attributed to the introduction of MoP. Metallic characteristic of MoP IO allows for better

electron mobility, resulting in lower photoluminescence intensity. 30% CdS/MoP IO photocatalyst shows the lowest photoluminescence intensity, indicating the recombination of photoexcited charge carriers could be suppressed effectively in this composite.

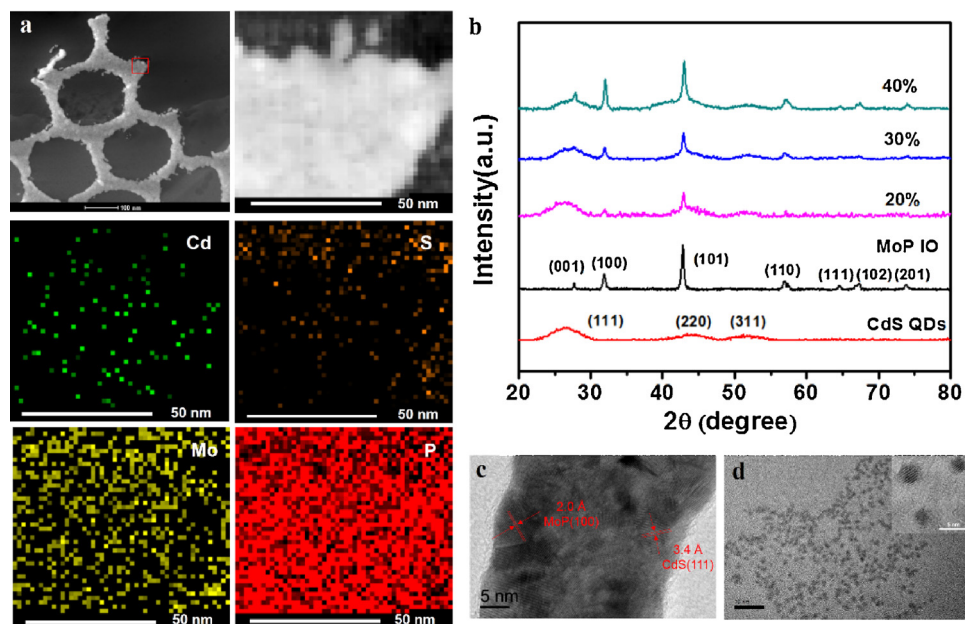


Fig. 3. (a) Elemental mapping of 30% CdS/MoP IO, (b) XRD patterns of CdS QDs, MoP IO and CdS/MoP IO, and (c, d) HRTEM images of 30% CdS/MoP IO and pure CdS QDs.

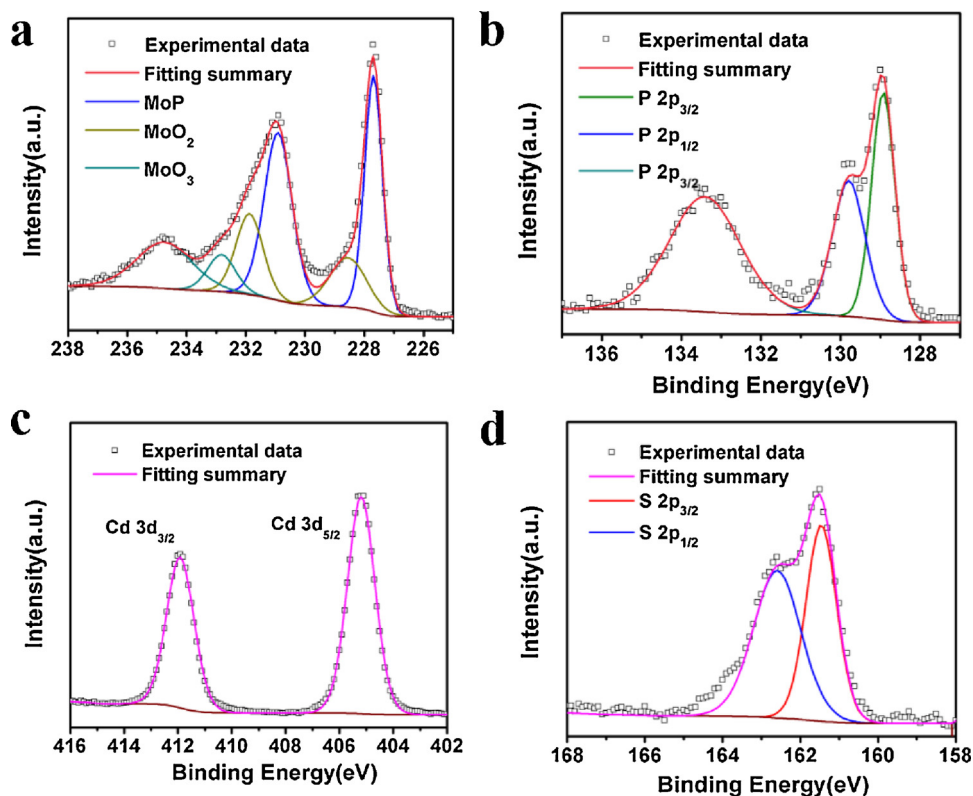


Fig. 4. XPS spectra of CdS/MoP IO (a) Mo 3d, (b) P 2p, (c) Cd 3d, (d) S 2p.

To investigate the photoelectrochemical behavior of all the samples under visible light illumination, photocurrent density measurement was carried out (Fig. 6a). When the loading amount of CdS quantum dots is 30%, the photocurrent density of CdS/MoP IO is the highest, which is 13 times that of CdS QDs. Besides, the photocurrent density of CdS/MoP IO decreases with the increase of cadmium sulfide quantum dots deposition, but it is still higher than the pure molybdenum phosphide inverse opal. Therefore, the depositing amount of CdS quantum dots has great impact on the photocatalytic activity of CdS/MoP IO, and the optimum amount of CdS QDs is 30%. Fig. 6b reveals the valence band edge XPS spectra of CdS QDs and MoP IO. The valence band edge of CdS QDs and MoP IO are located at 1.41 and -0.08 eV respectively.

3.3. Evaluation of photocatalytic activity of CdS/MoP IO

The photocatalytic activity of CdS/MoP IO is evaluated for phenol degradation under visible-light irradiation. The HPLC chromatograms of initial phenol and possible degradation intermediates produced

during the photocatalytic phenol degradation processes are shown in Figure S5a. Phenol, a typical intermediate product of degrading aromatic hydrocarbons, is difficult to remove by traditional degradation methods. As shown in Fig. 7a, phenol is stable under visible-light illumination without photocatalysts. In the presence of CdS QDs, only 37.4% of phenol is decomposed with 120 min irradiation. However, all the CdS/MoP IO samples show higher photocatalytic activities than pure CdS QDs. 81.8% of phenol can be removed by 20% CdS/MoP IO. 30% CdS/MoP IO exhibit the highest activity, and 97.5% of phenol is degraded in this case. About 93% of the TOC being mineralized by 30% CdS/MoP IO after 120 min of reaction is evidenced in Figure S5b. Further increase the content of CdS QDs, 40% CdS/MoP IO exhibit evidently decreased photocatalytic activity, resulting from serious agglomerates of CdS QDs. Such particle accumulation reduce the interface area between CdS and MoP IO and overlap their active sites, therefore inhibit the charge separation efficiency. The kinetic behaviors of CdS QDs and CdS/MoP IO follow first-order kinetics model, the rate constants of CdS QDs, 20% CdS/MoP IO, 30% CdS/MoP IO and 40% CdS/MoP IO are 0.0016, 0.0017, 0.0018 and 0.0015 min⁻¹ respectively.

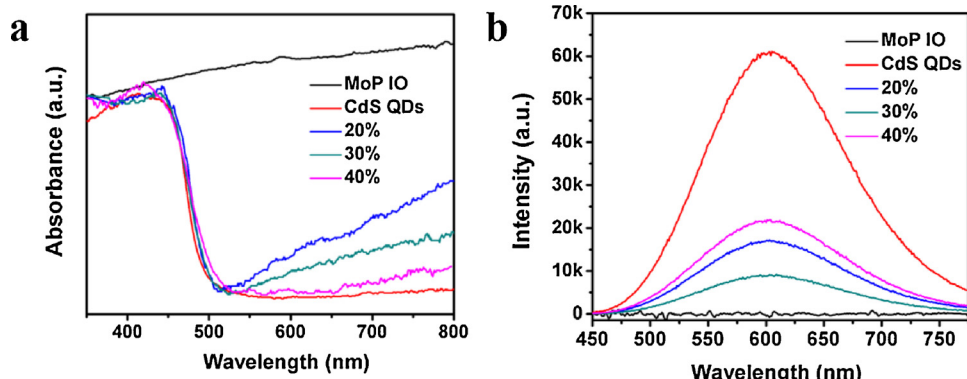


Fig. 5. (a) UV-vis diffuse reflectance spectra and (b) photoluminescence spectra of CdS QDs, MoP IO and CdS/MoP IO.

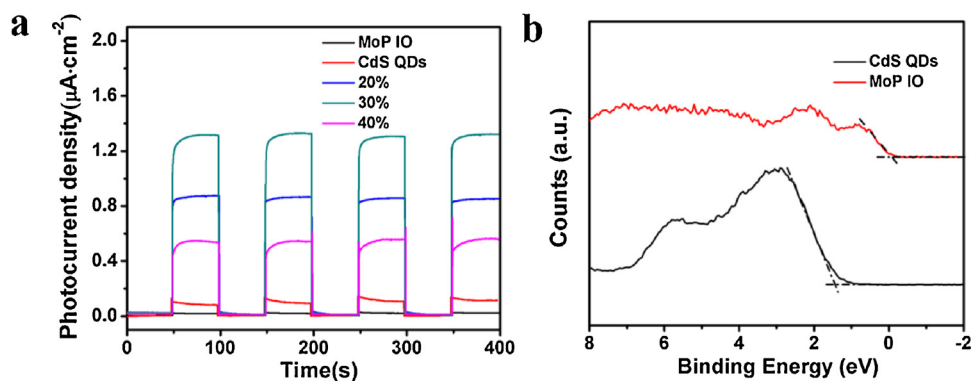


Fig. 6. (a) Photocurrent response of CdS QDs, MoP IO and CdS/MoP IO and (b) valence band XPS spectra of CdS QDs and MoP IO.

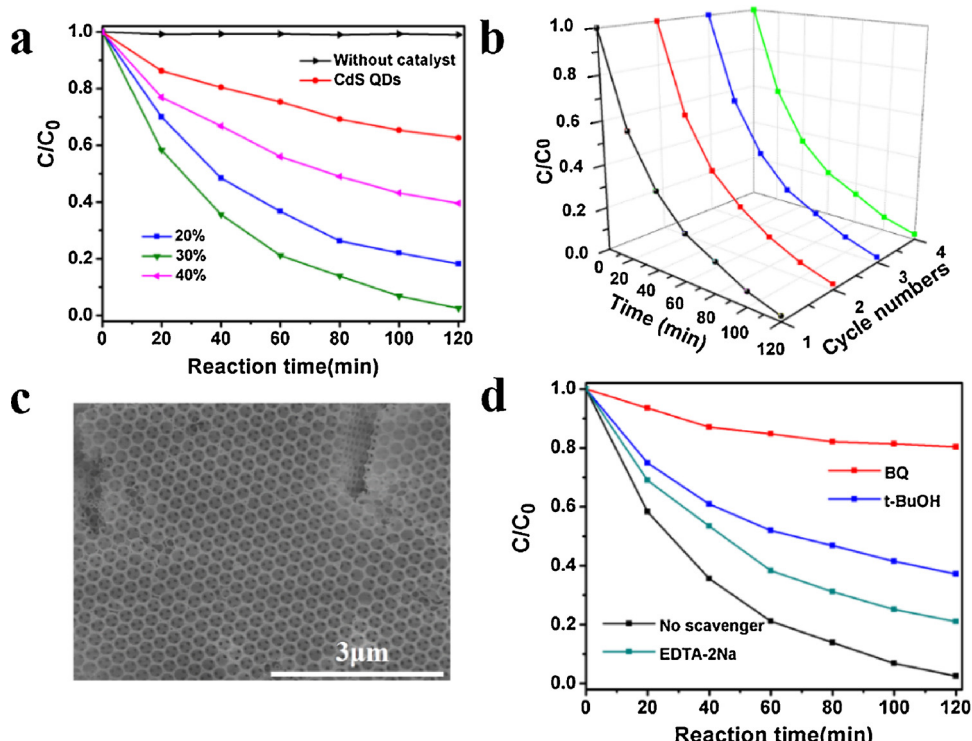


Fig. 7. (a) Phenol degradation curves for CdS QDs, MoP IO and CdS/MoP IO, (b) recycling performance of 30% CdS/MoP IO towards phenol degradation, (c) SEM image of 30% CdS/MoP IO after degradation cycling and (d) effect of scavengers on the degradation of phenol under visible-light illumination.

Table 1

Kinetic constants and correlation coefficients of CdS QDs and CdS/MoP IO for phenol degradation.

Samples	$k(\text{min}^{-1})$	R^2
CdS QDs	0.377×10^{-2}	0.975
20% CdS/MoP IO	1.435×10^{-2}	0.982
30% CdS/MoP IO	2.912×10^{-2}	0.976
40% CdS/MoP IO	0.758×10^{-2}	0.973

MoP IO are calculated to be 0.377×10^{-2} , 1.435×10^{-2} , 2.912×10^{-2} , 0.758×10^{-2} min^{-1} respectively (Table 1). To confirm the stability of 30% CdS/MoP IO, cycling degradation of phenol is examined as shown in Fig. 7b. The stability of 30% CdS/MoP IO is also tested by cycling experiment for 10 times. The photocatalytic efficiency of 30% CdS/MoP IO is shown in Figure S6 and there is no obvious photocatalytic activity loss during the process of phenol cyclic degradation. Inductively coupled plasma mass spectrometry (ICP-MS) is applied to determine the concentration of Cd²⁺ released in the solution

after photocatalytic degradation. The concentration of released Cd²⁺ is only around 5.84×10^{-3} mg/L after 12 h photocatalytic degradation, indicating the photocorrosion of CdS QDs can be effectively suppressed by the combination of CdS QDs with MoP IO. And XPS measurement (Figure S7) is applied to confirm the presence of sulfur in the non-oxidized form after photocatalytic degradation, further suggesting the photocorrosion of CdS is effectively inhibited. To test the structural stability, morphology of 30% CdS/MoP IO after 4 cycles is depicted in Fig. 7c. The ordered skeleton of MoP IO is maintained, suggesting the composite is structurally stable. The above results indicate that the introduction of MoP IO is probably beneficial to charge carrier transfer and subsequently enhances the photocatalytic activity of phenol degradation.

The mechanism of phenol photocatalytic degradation by CdS/MoP IO is elucidated by introducing p-benzoquinone (BQ, 1 mM), tert-butyl alcohol (t-BuOH, 1 mM) and ethylenediaminetetraacetate (EDTA-2Na, 1 mM) as $\cdot\text{O}_2^-$, $\cdot\text{OH}$ and holes scavengers for photocatalytic degradation, respectively (Fig. 7d). The addition of t-BuOH and EDTA-2Na to the reaction system results in moderate inhibition of phenol

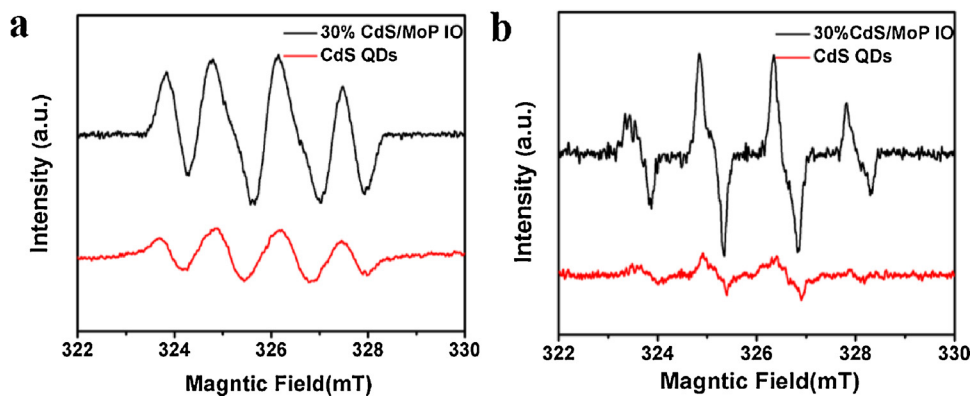
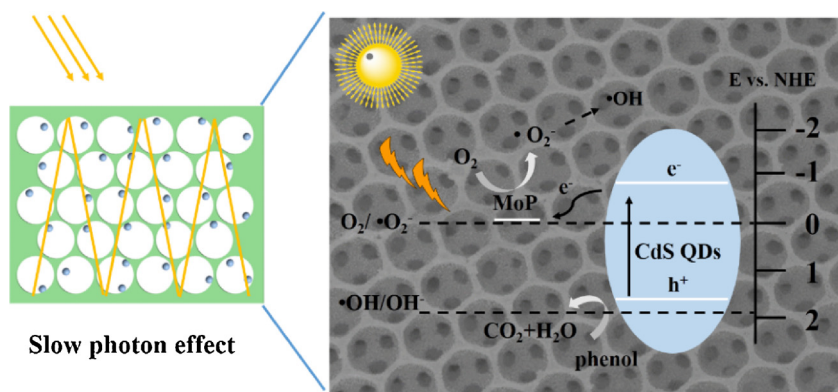


Fig. 8. EPR spectra of 30% CdS/MoP IO and pure CdS QDs (a) in methanol dispersion for DMPO-•O₂⁻ and (b) in water dispersion for DMPO-•OH under visible-light irradiation.

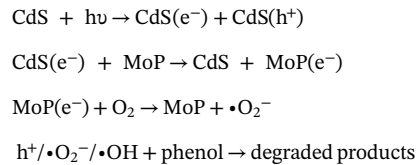


Scheme 2. Schematic diagram of photocatalytic phenol degradation under visible light irradiation with CdS/MoP IO.

decomposition. After adding BQ into the reaction system, the removal efficiency is significantly reduced to 20%. These results indicate that •O₂⁻, •OH, and holes are active species in photocatalytic degradation of phenol. To detect the signals of •O₂⁻ and •OH in 30% CdS/MoP IO and CdS QDs, EPR spin trap with DMPO technique is employed (Fig. 8). The characteristic four peaks of DMPO-•O₂⁻ species with intensity ratio of 1:1:1:1 is obviously detected under visible light irradiation, indicating the generation of •O₂⁻. Further, 30% CdS/MoP IO performs stronger •O₂⁻ signal, suggesting that •O₂⁻ radicals generated on the 30% CdS/MoP IO surface is more than that of pure CdS QDs. The peaks with intensity of 1:2:2:1 for DMPO-•OH adduct confirm the formation of •OH. The intensity of •OH radicals in CdS QDs is weak and more •OH are generated after the combination of MoP IO. Combined with the valence band XPS spectra of CdS QDs and MoP IO shown in Fig. 6b, a probable mechanism is put forward in Scheme 2.

When CdS/MoP IO is irradiated by visible light, the slow photon effect of inverse opals can effectively improve the optical absorption property due to its unique three-dimensional ordered structure. Subsequently, CdS quantum dots absorb photons, and produce photo-generated electrons and holes pairs. The photoexcited electrons can facilely transfer from the conduction band of CdS QDs to MoP Fermi level due to the good electron mobility of MoP, which effectively inhibit the recombination of charge carriers. Because the photoexcited holes in the valence band of CdS QDs (~ + 1.41 eV vs. NHE) is unable to directly oxidize hydroxyl groups into •OH radicals (E (•OH/OH⁻) = + 1.99 V, vs. NHE) for the more negative valence band potential, it is confirmed that the detected •OH are produced from •O₂⁻ by photochemical reaction (H₂O₂ + •O₂⁻ → •OH + OH⁻ + O₂²⁻) and •OH radicals are active species to oxide phenol in this paper. What's more, holes in the valence band of CdS QDs can directly degrade phenol to small molecules. Therefore, an effective photogeneration electrons and holes

separation can be achieved to enhance the photocatalytic efficiency. The photocatalytic process includes the equations as following:



4. Conclusion

In summary, a photocatalytic system has been constructed by depositing CdS QDs on the framework of MoP IO, and the photocatalytic activity is assessed by the degradation of phenol under visible light illumination. The highest rate constants of CdS/MoP IO for photocatalytic phenol degradation is 7.7 times higher than pure CdS QDs, and the possible mechanism is proposed. Three-dimensional ordered structure of CdS/MoP IO is beneficial to increase light adsorption ability. Excellent electrical conductivity of MoP facilitate the photoexcited electrons transfer from the conduction band of CdS to MoP Fermi level, which effectively reduce recombination of photoexcited electron-hole pairs and improve photocatalytic activity. CdS/MoP IO is a promising photocatalyst which has great potential for application in environment purification.

Acknowledgements

We thank Dr. Shengpeng Sun for kind help in total organic carbon measurement and discussion. We gratefully acknowledge the financial support provided by National Natural Science Foundation of China (51573122, 21722607, 21776190), Natural Science Foundation of the

Jiangsu Higher Education Institutions of China (17KJA430014, 17KJA150009), the National Key Technology R&D Program (2015BAG20B03-06), the Science and Technology Program for Social Development of Jiangsu (BE2015637) and the project supported by the Priority Academic Program Development of Jiangsu Higher Education Institutions (PAPD).

Appendix A. Supplementary data

Supplementary material related to this article can be found, in the online version, at doi:<https://doi.org/10.1016/j.apcatb.2018.07.010>.

References

- [1] J. Yao, H. Chen, F. Jiang, Z. Jiao, M. Jin, *J. Colloid Interf. Sci.* 490 (2017) 154–162.
- [2] J. Jiang, H. Wang, X. Chen, S. Li, T. Xie, D. Wang, *J. Colloid Interf. Sci.* 494 (2017) 130–138.
- [3] E. Saputra, S. Muhammad, H. Sun, A. Patel, P. Shukla, Z. Zhu, S. Wang, *Catal. Commun.* 26 (2012) 144–148.
- [4] W. Dong, F. Pan, L. Xu, M. Zheng, C.H. Sow, K. Wu, *Appl. Surf. Sci.* 349 (2015) 279–286.
- [5] A. Li, Q. Zhang, G. Zhang, J. Chen, Z. Fei, F. Liu, *Chemosphere* 47 (2002) 981–989.
- [6] P. Wu, Z. Liao, H. Zhang, J. Guo, *Environ. Int.* 26 (2001) 401–407.
- [7] H. Ma, X. Zhang, Q. Ma, B. Wang, *J. Hazard. Mater.* 165 (2009) 475–480.
- [8] S. Golbaz, A. Jafari, M. Rafiee, R. Kalantary, *Chem. Eng. J.* 253 (2014) 251–257.
- [9] Z. Li, M. Wu, Z. Jiao, B. Bao, S. Lu, *J. Hazard. Mater.* 114 (2004) 111–114.
- [10] C. Yang, Y. Qian, L. Zhang, J. Feng, *Chem. Eng. J.* 117 (2006) 179–185.
- [11] C. Yang, F. Li, M. Zhang, T. Li, W. Cao, *J. Mol. Catal. A Chem.* 423 (2016) 1–11.
- [12] Y. Zhao, F. Pan, H. Li, T. Niu, G. Xu, W. Chen, *J. Mater. Chem. A* 1 (2013) 7242–7246.
- [13] F. Xiao, J. Miao, H. Wang, H. Yang, J. Chen, B. Liu, *Nanoscale* 6 (2014) 6727–6737.
- [14] R. Zhang, X. Wang, J. Song, Y. Si, X. Zhuang, J. Yu, *J. Mater. Chem. A* 3 (2015) 22136–22144.
- [15] Q. Xie, H. Zhou, Z. Lv, H. Liu, H. Guo, *J. Mater. Chem. A* 5 (2017) 6299–6309.
- [16] C. Cheng, S.K. Karuturi, L. Liu, J. Liu, H. Li, L. Su, *Small* 8 (2012) 37–42.
- [17] P. Wang, T. Wu, C. Wang, J. Hou, J. Qian, Y. Ao, *ACS Sustain. Chem. Eng.* 5 (2017) 7670–7677.
- [18] J. Ran, J. Yu, M. Jaroniec, *Green Chem.* 13 (2011) 2708.
- [19] J. Zhang, S.Z. Qiao, L. Qi, J. Yu, *Phys. Chem. Chem. Phys.* 15 (2013) 12088–12094.
- [20] Z. Fang, Y. Wang, J. Song, Y. Sun, J. Zhou, R. Xu, *Nanoscale* 5 (2013) 9830–9838.
- [21] D. Neo, C. Cheng, S. Stranks, S. Fairclough, J. Kim, A. Kirkland, *Chem. Mater.* 26 (2014) 4004–4013.
- [22] H. Kim, T. Kim, I. Kim, S. Wang, *Adv. Funct. Mater.* 21 (2011) 3111–3118.
- [23] Y. Zhu, Z. Chen, T. Gao, Q. Huang, F. Niu, L. Qin, *Appl. Catal. B: Environ.* 163 (2015) 16–22.
- [24] C. Zhai, M. Zhu, F. Pang, D. Bin, C. Lu, M.C. Goh, *ACS Appl. Mater. Interf.* 8 (2016) 5972–5980.
- [25] Q. Wang, J. Li, Y. Bai, X. Lu, Y. Ding, S. Yin, *J. Photochem. Photobiol. B* 126 (2013) 47–54.
- [26] S. Yin, J. Han, Y. Zou, T. Zhou, R. Xu, *Nanoscale* 8 (2016) 14438–14447.
- [27] Q. Yue, Y. Wan, Z. Sun, X. Wu, Y. Yuan, P. Du, *J. Mater. Chem. A* 3 (2015) 16941–16947.
- [28] Z. Sun, H. Zheng, J. Li, P. Du, *Energy Environ. Sci.* 8 (2015) 2668–2676.
- [29] S. Cao, Y. Chen, C.J. Wang, P. He, W.F. Fu, *Chem. Commun.* 50 (2014) 10427–10429.
- [30] J. Tian, N. Cheng, Q. Liu, W. Xing, X. Sun, *Angew. Chem. Int. Edit.* 54 (2015) 5493–5497.
- [31] B. Qiu, Q. Zhu, M. Xing, J. Zhang, *Chem. Commun.* 53 (2017) 897–900.
- [32] H. Cheng, X.J. Lv, S. Cao, Z.Y. Zhao, Y. Chen, W.F. Fu, *Sci. Rep.* 6 (2016) 19846.
- [33] Y. Lu, H. Yu, S. Chen, X. Quan, H. Zhao, *Environ. Sci. Technol.* 46 (2012) 1724–1730.
- [34] M. Wu, J. Jin, J. Liu, Z. Deng, Y. Li, O. Deparis, *J. Mater. Chem. A* 1 (2013) 15491.
- [35] C. Li, X. Zhu, H. Zhang, Z. Zhu, B. Liu, C. Cheng, *Adv. Mater. Interfaces* 2 (2015) 1500428.
- [36] X. Du, J. He, *J. Appl. Polym. Sci.* 108 (2008) 1755–1760.